Source of Acquisition
NASA Goddard Space Flight Center

Popular summary for

"The plane-parallel albedo bias of liquid clouds from MODIS observations"

by Lazaros Oreopoulos, Robert F. Cahalan, and Steven Platnick

submitted to J. of Climate

In our most advanced modeling tools for climate change prediction, namely General Circulation Models (GCMs), the schemes used to calculate the budget of solar and thermal radiation commonly assume that clouds are horizontally homogeneous at scales as large as a few hundred kilometers. However, this assumption, used for convenience, computational speed, and lack of knowledge on cloud small scale variability, leads to erroneous estimates of the radiation budget. This paper provides a global picture of the solar radiation errors at scales of approximately 100 km due to warm (liquid phase) clouds only. To achieve this, we use cloud retrievals from the instrument MODIS on the Terra and Aqua satellites, along with atmospheric and surface information, as input into a GCM-style radiative transfer algorithm. Since the MODIS product contains information on cloud variability below 100 km we can run the radiation algorithm both for the variable and the (assumed) homogeneous clouds. The difference between these calculations for reflected or transmitted solar radiation constitutes the bias that GCMs would commit if they were able to perfectly predict the properties of warm clouds, but then assumed they were homogeneous for radiation calculations. We find that the global average of this bias is ~2-3 times larger in terms of energy than the additional amount of thermal energy that would be trapped if we were to double carbon dioxide from current concentrations. We should therefore make a greater effort to predict horizontal cloud variability in GCMs and account for its effects in radiation calculations.

The plane-parallel albedo bias of liquid clouds from MODIS observations

Lazaros Oreopoulos[1,2], Robert F. Cahalan[2,1], and Steven Platnick[2,1]

1. Joint Center for Earth Systems Technology, University of Maryland Baltimore County, Baltimore, MD

2. Laboratory for Atmospheres, NASA Goddard Space Flight Center, Greenbelt, MD

Submitted to the Journal of Climate

August 2006

Corresponding author address:
Lazaros Oreopoulos
NASA-GSFC
Code 613.2
Greenbelt, MD 20771

Abstract

We present the global plane-parallel shortwave radiation bias of liquid clouds for two months, July 2003 and January 2004. The optical properties needed to perform the bias calculations, specifically gridded (1°x1°) daily means, marginal histograms, and joint histograms of cloud optical thickness and effective radius come from the operational MODIS Terra and MODIS Aqua Level-3 datasets. These data, along with ancillary surface albedo and atmospheric information consistent with the MODIS retrievals, are inserted into a broadband, shortwave radiative transfer model to calculate the fluxes at the atmospheric column boundaries. The Plane-Parallel Homogeneous (PPH) calculations are based on the mean cloud properties, while Independent Column Approximation (ICA) calculations are based either on 1-D marginal histograms of optical thickness or the 2-D (joint) histograms of optical thickness and effective radius. Two types of biases are examined: (1) the bias due to the horizontal inhomogeneity of optical thickness alone (the effective radius is set to the grid mean value); and (2) the bias due to simultaneous variations of optical thickness and effective radius as derived from their joint histograms. The geographical and seasonal patterns of these biases are given for the entire solar spectrum, while global values are also shown separately for the combined ultraviolet-visible (UV-VIS, < 0.7 μm) and near-infrared (NIR, > 0.7 μm) portions of the spectrum. We find that the global bias of albedo (liquid cloud portion of the gridpoints only) is ~+0.03 which corresponds to roughly 8% of the global liquid cloud albedo, and is only modestly sensitive to the inclusion of horizontal effective radius variability, season, or time of day. This albedo bias translates to ~7-8 Wm^{-2} of bias (i.e., stronger negative values) in the global shortwave cloud radiative forcing, assuming homogeneous conditions for the fraction of the gridpoint not covered by liquid clouds, while zonal averages can reach values as high as 14 Wm^{-2}. The fractional contribution of the UV-VIS portion of the spectrum to the albedo bias is only marginally higher than the fraction of solar energy in the band. Finally, the broadband atmospheric absorption bias is about an order of magnitude smaller than the albedo bias. The substantial magnitude of the plane-parallel bias in reflected and transmitted flux stresses the importance of predicting subgrid variability in GCMs and accounting for its effects in cloud-radiation interactions.

1. Introduction

The bias in solar radiative fluxes within a model or other large-scale grid due to the assumption of horizontal homogeneity in cloud optical thickness τ (Plane-Parallel Homogeneous–PPH– bias) received a great amount of attention following the publication of the study by Cahalan et al. (1994), even though its existence and potential importance was stressed in earlier publications (Harshvardhan and Randall, 1985; Stephens 1988). Cahalan et al. provided a theoretical framework for the PPH bias using a fractal cloud model, but restricted the quantitative analysis of cloud inhomogeneity on marine stratocumulus clouds with properties described by surface microwave radiometer observations. Cloud microphysics (i.e., droplet effective radius, r_e) was assumed constant (r_e=10 μm), surface and atmospheric effects were neglected, and the radiative transfer did not extend beyond monochromatic calculations. For typical marine stratocumulus observed during the First ISCCP (International Satellite Cloud Climatology Project) Regional Experiment (FIRE), Cahalan et al. found a value of +0.09 as representative of the PPH albedo bias at visible wavelengths. Subsequent observationally-based work (Barker et al. 1996, Oreopoulos and Davies 1998; Pincus et al., 1999; Rossow et al. 2002) provided additional estimates of average PPH albedo bias that ranged from +0.02 to +0.3 depending on the spectral range, cloud type, spatial resolution of the satellite observations, and area over which clouds were assumed homogeneous. Bias estimates of reflected solar flux (or equivalently shortwave cloud radiative forcing) were also derived for cloud fields provided by the Multiscale Modeling Framework (Khairoutdinov et al., 2005) by Räisänen et al., (2004) and Oreopoulos et al. (2004), but these were limited to

very short (24 hours) time periods, and included compensating errors emanating from the cloud fraction overlap assumptions of the radiative transfer codes.

The present study provides the most extensive hitherto estimates of PPH bias for liquid clouds. Specifically, we present global distributions of broadband (BB) flux bias that are based on MODIS liquid water cloud retrievals for two entire months, and account for the effects of atmospheric absorption and surface reflectance by use of the same ancillary data sets used in the retrievals. Since the calculations are broadband and refer to the entire atmospheric column, estimates of the bias in solar radiation absorbed by the surface and atmosphere are examined as well. We also take advantage of the availability of joint optical τ-r_e histograms to compare the total bias due to the combined τ-r_e variability with those solely due to τ variations.

The dataset and computational details are provided in the next section; results are presented in section 3 and conclusions given in section 4.

2. Dataset and radiative transfer calculations

We use daily MODIS Level-3 1° resolution gridded data) from both the Terra (~1030 local time overpass) and Aqua (~1330 overpass) satellites; these datasets will be referred to by their product names MOD08_D3 and MYD08_D3, respectively. This high-level dataset, obtained from the Collection 4 processing stream, contains the mean daily values of optical thickness ($\overline{\tau}$), effective radius ($\overline{r_e}$), cloud fraction of successful cloud retrievals, and solar zenith angle (SZA), as well as marginal one-dimensional and joint histograms of τ and r_e (King et al., 2003). For liquid clouds used in this study, the marginal 1D histograms of τ are resolved in 45 bins; the joint 2D histograms of τ and r_e

are resolved in 110 bins (11 for τ and 10 for r_e). Except for high latitudes where gridpoints can be revisited within the same day due to orbital swath overlap, the daily histograms mainly represent the spatial variability of τ and r_e within the 1°x1° gridpoint.

The radiative transfer calculations yielding daily atmospheric column albedo, transmittance, and absorptance at the mean SZA of the gridpoint are performed with a modified version of the shortwave (SW) Column Radiation Model (CORAM) described by Chou et al. (1998). The model can provide the flux profile of the entire atmospheric column, either over the entire solar spectrum (0.2–5.0 μm), or over the ultraviolet-visible (UV-VIS, 0.2–0.7 μm) and near-infrared (NIR, 0.7–5.0 μm) bands separately. It can account for molecular, aerosol and cloud absorption and scattering, and surface reflection with and without a vegetation canopy. Since our calculations are for the cloudy portion of the gridpoint only, and assume single-layer clouds, the cloud fraction overlap assumptions of the model are not used. To isolate the albedo and transmittance of the clouds themselves, one can easily switch off the atmosphere and surface (i.e., clouds in a vacuum). We show results for both types of calculations (full-column and cloud in a vacuum) in section 3. For full-column calculations, the values of surface albedo and the concentrations of active atmospheric absorbers, H_2O (profile), O_3 (column amount), and CO_2 are required (aerosols are neglected in our calculations).

Ancillary surface spectral albedo comes from the identical data sources and methods used in the operational MODIS cloud retrievals. The snow-free and permanent snow/ice albedo is the 5-year climatology of Moody et al. (2005), which uses an ecosystem-dependent temporal interpolation technique to fill missing or seasonally snow-covered data in the operational MODIS Terra surface albedo product (MOD43B3). The data are

provided in a 1 arc minute equal-angle grid with the seasonal cycle resolved in 16-day periods. Snow and ice scenes are identified with the snow/ice index from National Oceanic and Atmospheric Administration (NOAA) microwave-derived daily 0.25° Near Real-Time Ice and Snow Extent (NISE) dataset. Spectral albedos for non-permanent snow on land surfaces are taken from lookup tables populated by seasonal MOD43B3 albedos aggregated by the MODIS Terra ecosystem product (MOD12Q1). Sea-ice albedo is derived from a combination of permanent snow/ice and open-ocean albedo along with an estimate for the melt-season transition. In all cases, we use the diffuse ("white-sky) albedo for the broad 0.3–0.7 μm and 0.7–5.0 μm bands which roughly correspond to the UV-VIS and NIR bands of the Chou et al. (1998) model.

Atmospheric profiles of temperature and water vapor are resolved into 16 layers extending from 1000 to 10 mb and come from the National Center for Environmental Prediction (NCEP) Global Data Assimilation System (GDAS) product (Derber et al., 1991). This data set is identical to the one used in the operational MODIS retrievals. The product also provides total (column) ozone concentration. The CO_2 concentration is set at 370 ppm. The cloud is placed in the layer whose top temperature is closest to the mean cloud top temperature ($\overline{T}_c$) as derived from the joint histogram of liquid cloud τ and T_c.

A significant modification to our version of the CORAM is the introduction of a new method of calculating cloud optical properties (extinction, single-scattering albedo, asymmetry parameter). It essentially consists of look-up tables of these properties as a function of r_e for the four broad spectral intervals (one in the UV-VIS and three in the NIR) of the model. These look-up tables are based on the tabulated values of Hu and Stamnes (1993) and allow calculation of optical properties for $r_e > 20$ μm which was not

possible with the original Chou et al. (1998) parameterization. Since the visible values of τ from the MODIS dataset are not sufficient for the BB radiative transfer calculation, we adopt the following methodology to obtain the spectral values of τ for the four broad intervals of model: first, we assume that the τ values in the MODIS dataset correspond to the first spectral interval of the Chou et al. (1998) model; then, for the associated r_e retrieval, we find the extinction corresponding to the spectral interval and combine it with τ to obtain the liquid water path (LWP). This value of LWP is subsequently used with the appropriate extinction coefficient for the other three spectral intervals to obtain spectral τ values.

For the mean SZA of a gridpoint on a particular day, three different types of albedo (R) are calculated: (1) using the $\overline{\tau}$ and $\overline{r_e}$ values of the gridpoint (the PPH albedo R_{PPH}); (2) using the marginal histogram of τ and the gridpoint mean value of effective radius $\overline{r_e}$ (type 1 ICA albedo R_{ICA1}), i.e., an albedo obtained from multiple albedo calculations weighted by the relative frequency in each τ bin; and (3) using the 2D histogram (type 2 ICA albedo R_{ICA2}), i.e., an albedo obtained from multiple albedo calculations weighted by the relative frequency in each (τ, r_e) bin. The albedo calculated with the first method minus that calculated with the second gives the classic plane-parallel albedo bias with constant microphysics (B_1^R). The albedo calculated with the first method minus that that calculated with the third gives the albedo bias due to horizontal variations of both τ and r_e (B_2^R). Mathematically, the biases can be expressed as follows:

$$B_1^R\left(\overline{\tau},\overline{r}_e,\nu_\tau,\mu_0\right)=R_{PPH}-R_{ICA1}\equiv\mathbf{R}\left(\overline{\tau},\overline{r}_e,\mu_0\right)-\int\mathbf{R}\left(\tau,\overline{r}_e,\mu_0\right)p(\tau)d\tau \quad (1a)$$

$$B_2^R\left(\overline{\tau},\overline{r}_e,\nu_{\tau,r_e}\mu_0\right)=R_{PPH}-R_{ICA2}\equiv\mathbf{R}\left(\overline{\tau},\overline{r}_e,\mu_0\right)-\int\int\mathbf{R}\left(\tau,r_e,\mu_0\right)p(\tau,r_e)d\tau dr_e \quad (1b)$$

where μ_0 is the cosine of the solar zenith angle, ν is a measure of either τ or joint τ-r_e variability (e.g., a shape parameter of the 1-D probability density function $p(\tau)$ or the 2-D probability density function $p(\tau, r_e)$), and **R** is the reflectance function (e.g., the analytical solution of the two-stream approximation). The dependencies of the albedo bias on molecular absorption, Rayleigh scattering, and surface albedo are not explicitly shown in the above equations, so Eqs. (1a) and (1b) are strictly accurate for clouds in a vacuum only. It is understood, however, that all these factors (assumed to be homogeneous within the 1° gridpoint) are accounted for in all our calculations for the combined atmospheric column-surface system. The ICA calculations are subject to errors that due to the discretization of the 1D and 2D histograms, but these errors are expected to be of random nature.

The albedo bias calculations are performed for every day of the month in each gridpoint and are then averaged to monthly values using the gridpoint cloud fraction of successful liquid water retrievals as a weight. Due to the generally larger uncertainties in the retrievals and parameterization of wide-band optical properties of ice clouds, we restrict the current analysis to liquid water clouds only. We plan to revisit the issue of the ice cloud albedo bias in the future, following derivation of wide-band optical properties for our radiative transfer model that are consistent with the ice crystal size distributions used in the MODIS retrievals.

3. Results

As described previously, we have performed a large number of bias calculations covering the entire portion of the globe for which illumination conditions allow MODIS cloud property retrievals. The bias calculations were performed for both full (atmosphere-surface) columns containing clouds, and clouds only in vacuum, for both joint τ-r_e or only τ variability, for both MODIS Terra and MODIS Aqua, and for both July 2003 and January 2004. Most the results shown below are for full column calculations (when this is not the case, it will be explicitly stated) and are from MODIS Terra with τ-only variability. However, differences between platforms, and method of calculation are discussed.

The top panel of Fig. 1 shows global (area–weighted) monthly-averaged PPH albedo, and PPH biases (B_1^R and B_2^R) for liquid clouds from MODIS Terra and MODIS Aqua Level-3 (cloudy portion of gridpoints only). The global PPH albedo bias due to only optical thickness variations is ~+0.03 and differs only slightly between the two months and between morning (Terra) and afternoon (Aqua); the July bias is a somewhat higher than the Januay bias, and the Aqua bias is a little higher than the Terra bias. The biases are ~8% of the global PPH albedo (white bars). Interestingly, the bias tends to be larger when the albedo is smaller, i.e., MODIS Aqua for July exhibits the largest relative bias (+8.5%) while MODIS Terra for January the smallest (+7.5%). This may be due in part to the tendency of cloud albedo to be smaller and the bias to be larger when the SZA is lower (July exhibits on average low SZAs), all else remaining constant. Cahalan et al. (1994) attributed the decrease of the PPH bias with SZA to the reduced albedo contrast at

oblique illuminations between the optically thinner and thicker clouds of an optical thickness distribution when $\overline{\tau}$ is not too small.

The bottom panel of Fig. 1 shows the corresponding global PPH biases of reflected solar flux at TOA derived by averaging biases for the entire gridpoint (i.e., including clear sky). This is equivalent to the absolute value of the bias B^{SWCRF} in (negative) SW Cloud Radiative Forcing *SWCRF* since

$$SWCRF = F^{clr} - F^{all-sky} = A_c(F^{clr} - F^{cld}),$$

where the all-sky flux ($F^{all\text{-}sky}$) is expressed as the cloud fraction (A_c)–weighted average of the clear and cloudy sky fluxes (F^{clr} and F^{cld}, respectively):

$$F^{all-sky} = (1 - A_c)F^{clr} + A_c F^{cld}.$$

Therefore,

$$B^{SWCRF} = SWCRF_{PPH} - SWCRF_{ICA} = -A_c(F^{cld}_{PPH} - F^{cld}_{ICA}) = -A_c B^F, \qquad (2)$$

where $B^F = F^{cld}_{PPH} - F^{cld}_{ICA}$ is the bias in reflected solar flux for the cloudy portion of the gridpoint. The absolute values of B^{SWCRF} solely due to optical thickness variations range from 7.1 Wm^{-2} (MODIS Terra, July) to 8.3 Wm^{-2} (MODIS Aqua, January). The magnitude of these values obviously depends strongly on the amount of solar insolation which depends on the SZA and the Earth-Sun distance. It is apparent that the PPH *SWCRF* bias of liquid clouds is a substantial fraction of the global *SWCRF* due to all types of clouds (approximately -50 Wm^{-2} according to Kiehl and Trenberth 1997). However, since our albedo and insolation are calculated at the time of satellite overpasses

which are close to local solar noon, our values, strictly speaking, are not proper diurnal averages, and may represent overestimates of the *SWCRF* bias.

Figure 1 also shows albedo and flux biases for the combined τ-r_e variability, When r_e variability is also accounted for, the albedo biases decrease by ~0.001-0.003 (~4.5-9.6%) (the largest value corresponds to MODIS Terra for July). In terms of reflected flux or *SWCRF* bias, the effect of r_e spatial variability is ~0.5 to 0.8 Wm^{-2} (largest value for MODIS Terra, January). These numbers suggest a more modest effect of r_e variations compared to previous studies (Räisänen et al., 2003; Barker and Räisänen, 2004). However, these prior results are not directly comparable to ours for the fundamental reason that in those studies the other cloud property available was not τ, but cloud water (from aircraft measurements in Räisänen et al., 2003 and from the Multi-Scale Modeling Framework model in Barker and Räisänen, 2004). As a result, the inferred τ variability in those studies was the aggregate of combined r_e and water content variability (in other words, r_e variability was also driving cloud extinction variability). Here the τ variability is given from the simultaneous, combined τ-r_e MODIS retrievals so that r_e variability is only affecting asymmetry factor and single-scattering albedo variability. To put it another way, the contribution to the PPH bias arising from r_e spatial variability is, in our case, due to the concavity of the albedo vs. r_e curve under constant τ, which is weak (Fig. 2, solid line). In contrast, the concavity of the albedo vs. r_e curve under constant LWP is significant (Fig. 2, dotted line), and magnifies the influence of r_e variations in Räisänen et al., and Barker and Räisänen.

While Fig. 1 indicates that the global values of PPH bias are very similar between and July, substantial differences can be seen between hemispheric land and

ocean values. Figure 3 shows hemispherically-averaged PPH albedos (top panel) and B_1^R values (bottom panel) separately for land and ocean areas of the Northern Hemisphere (NH) where there is a more balanced ratio of land and ocean gridpoints. On a hemispheric basis, the July and January biases are similar only over land. The oceanic biases increase in January compared to July (and become larger than their counterparts over land), most likely due to the substantial increase in the inhomogeneity of marine clouds (Oreopoulos and Cahalan, 2005); the change of continental cloud inhomogeneity is much smaller (Oreopoulos and Cahalan, 2005).

Figure 3 also shows the impact of including surface albedo and atmospheric absorption in the albedo/bias calculations. Over land, an apparent cancellation between the brightening effect of surface albedo and the darkening effect of atmospheric absorption occurs. Over the dark ocean surface however, atmospheric absorption dominates and the full-column albedo is lower than the albedo of clouds in vacuum. Still, for both ocean and land, the PPH bias is smaller for full-column calculations. This simply reflects the fact that the contribution of clouds to the TOA albedo is smaller when atmospheric and surface effects are accounted for.

Figure 4 shows the geographical distribution of monthly-averaged PPH albedo bias (weighted by liquid cloud fraction) solely due to optical thickness variations (B_1^R bias) for MODIS Terra. The top and bottom panels are for July 2003 and January 2004, respectively. The bias corresponds only to the portion of the Level-3 1°x1° gridpoints filled with liquid clouds. Atmospheric and surface effects are included in the manner described in the previous section. A distinct contrast between the winter and summer hemispheres is evident. The albedo bias assumes large values in the winter hemisphere

oceans, small values in the summer hemisphere oceans, and larger values over land in the NH summer compared to NH winter. A comparison of albedo bias maps between full-column and clouds in a vacuum calculations (not shown) reveals that a significant reduction of albedo bias in NH winter continental masses occurs because of the increase in (often snow-covered) surface albedo. The same effect is especially prominent over Antarctica where the surface albedo is such a large contributor to the full-column albedo that the albedo bias is all but eliminated.

As expected, and as already implied previously, the geographical distribution of albedo bias correlates with the geographical distribution of the inhomogeneity parameter χ (ratio of logarithmic to linear τ mean) shown in Fig. 7 of Oreopoulos and Cahalan (2005): large values of albedo bias generally correspond to small values of χ (large cloud inhomogeneity) and vice-versa. Figure 5 collects the PPH biases and χ values of these two plots for July 2003 and displays them in the form of a scatterplot (i.e., each point represents a MODIS Terra July 2003 1°x1° gridpoint where it was possible to make liquid cloud χ and bias estimates). While the expected anticorrelation is present, there is also considerable scatter, not only because of the averaging at monthly scales, but also because of the influence of a host of other factors besides inhomogeneity (values of mean optical thickness, SZA, and surface albedo, strength of atmospheric absorption and scattering) on the albedo bias value. For example, gridpoints in the NH near-equatorial and subtropical central Pacific assume small albedo bias values (~+0.005–+0.02) despite χ values in the range of 0.6-0.7. This is because of the small values of $\overline{\tau}$ (~5) (making the dependence of albedo on optical thickness quasi-linear). Moreover, if the bias is expressed in units of cloud radiative forcing (see Eq. (2) above) the small liquid phase

cloud fraction would also tend to keep the bias values low despite the large amounts of insolation. The surface albedo in this case of marine clouds has a minimal effect on the PPH bias.

The top panel of Fig. 6 plots the normalized frequency of occurrence distributions of monthly-averaged B_1^R and B_2^R biases from MODIS Terra. These distributions where constructed by binning all available monthly-averaged gridpoint biases for the two months. Seasonal differences and differences between the two type of biases can be seen. The seasonal differences are primarily due to differences in illumination geometry and cloud inhomogeneity. The January histogram has a well-defined peak at an albedo bias of ~+0.024, while for July the frequency of occurrence around these values is smaller by about 30%, and a bimodal behavior can be seen. PPH albedo biases in the range between +0.03 and +0.06, on the other hand, are observed in many more gridpoints in July. The first peak in the January distribution is attributed to Antarctica gridpoints where the high surface albedos cause dramatic reductions in the PPH bias (distributions of biases calculated assuming black surface are devoid of this peak). Once again, it becomes apparent that the global values of Fig. 1 do not tell the whole albedo bias story: the nearly equal global values of PPH albedo bias for MODIS Terra in January and July (+0.0286 vs. +0.0292) come from two glaringly different distributions. The counterpart histograms including r_e variability have the same shape as those for only τ variability, but are shifted slightly to the left suggesting that the reduction of PPH bias is more or less uniform, consistent with the earlier interpretation of the relationship between r_e variations and albedo bias.

The bottom panel of Fig. 6 plots the normalized frequency of occurrence distributions of monthly-averaged PPH albedo bias from MODIS Terra and MODIS Aqua solely due to optical thickness variations (B_1^R bias). The January distribution for morning and afternoon are more similar than for July. This probably reflects the greater diurnal variability of continental clouds compared to marine clouds during the summer: the land-dominated NH exhibits a greater cloud variability in the summer compared to the ocean-dominated SH. The greater albedo bias for Aqua is consistent with the larger values of inhomogeneity (smaller values of χ) found in Oreopoulos and Cahalan (2005).

The bottom panel of Fig. 7 shows the zonal variation of monthly-averaged PPH bias (due to liquid cloud optical thickness variations only) in TOA reflected solar flux (F) for entire 1°x1° gridpoints (i.e., including clear skies). It is calculated as the product of the zonal flux bias of the cloudy portion of the gridpoint and the zonal cloud fraction, and, as explained above, is equivalent to the absolute value of the bias in *SWCRF*. The top panel is taken from Oreopoulos and Cahalan (2005) (the top panel of their Fig. 4) and shows the zonal variation of monthly-averaged χ for liquid clouds observed from MODIS Terra and MODIS Aqua for July 2003 and January 2004. The PPH flux bias varies considerably with latitude and the zonal-averages reach values as high as 14 Wm^{-2} in the midlatitudes of the SH during January. This maximum does not correspond to the maximum in inhomogeneity (minimum in χ in the top panel) or albedo bias (not shown). Rather, it is driven by large values in cloud fraction and large values in insolation. Actually, the fact that the amount of incident solar energy and the cloud fraction have a big influence on the values PPH flux bias (absolute *SWCRF* bias) is one of the primary reasons that there is no apparent correlation between the zonal patterns of bias and χ.

The PPH bias for transmittance T (B^T) can be defined similarly to the PPH bias for reflectance B^R given by Eq. (1). The PPH bias of atmospheric absorptance A is simply given by:

$$B^A = -B^N - B^R \tag{3}$$

where

$$A = 1 - T(1 - a_{sfc}) - R \equiv 1 - N - R$$

a_{sfc} is the surface albedo, N=T(1-a_{sfc}) is the solar flux absorbed at the surface, and B^N is the PPH bias of N. B^T and B^N are negative and in most cases larger in absolute value than B^R. This yields positive values of B^A.

Figure 8 compares global values of B^R ("TOA") and $-B^N$ ("SFC") from MODIS Terra July 2003 data. The top panel shows BB PPH biases. Once again, significantly larger biases are found when atmospheric and surface effects are omitted ("vac" legend). In the case of atmospheric effects, this is because the column albedo decreases due to molecular absorption (prevailing over Rayleigh scattering), and results in bias decreases that scale by approximately the same factor. In the case of the surface, the reduction in bias is because the contribution of the cloud albedo to the column albedo is smaller than in the case of a black surface, so any changes in the cloud albedo (such as due to inhomogeneity) will be felt less severely at the TOA. Another consequence of atmospheric and surface albedo effects is that the difference between $-B^N$ and B^R, i.e., B^A from Eq. (3), also decreases. But even for clouds in a vacuum, the global value of B^A is still much smaller than B^R and $-B^N$.

B^A is rarely greater than 10% of B^R as shown in Fig. 9 depicting the correlation between monthly-averaged B_1^R and B_1^A for clouds in a vacuum (top) and for clouds embedded in the full surface-atmosphere column system (bottom). Each point in the plot is a gridpoint for which bias estimates where possible for MODIS Terra July 2003 data. The correlation is much better for vacuum (coefficient of linear correlation r=0.81) than for full-column calculations (r=0.52). This reflects the fact that total atmospheric absorptance (including clouds) does not correlate in a simple manner with absorptance due to clouds only since clouds absorb solar radiation that would have otherwise been available for absorption by atmospheric water vapor. Also, note that the cloud absorptance bias is larger than the atmospheric absorptance bias. This echoes the results of the bottom panels of Fig. 3 and the bottom panel of Fig. 8 (discussed below) showing albedo biases with and without atmospheric and surface effects.

The bottom panel of Fig. 8 shows the ratio of UV-VIS PPH biases over total (broadband) biases for the cases considered in the top panel of that figure. The horizontal line indicates the fraction of solar energy in the UV-VIS region (first band of the CORAM). For reflected flux, the largest contribution to the bias comes from the UV-VIS portion of the spectrum. Also, the contribution is actually slightly larger when r_e variability is accounted for and atmospheric/surface effects neglected. For transmitted flux (absorbed at the surface), the largest contribution comes from the NIR. Due to the spectral dependence of molecular absorption/scattering and surface albedo, a straightforward interpretation of UV-VIS and NIR relative contributions to the total bias is only possible for clouds in a vacuum. The UV-VIS portion of the spectrum has a greater relative contribution to the BB albedo bias because the convexity of the UV-VIS

albedo curve is greater than that for the NIR. The opposite is true for transmittance and the concavity of the corresponding curve. But the proportionally greater contribution of NIR transmittance bias to the BB transmittance bias is also expected from energy conservation considerations: with no cloud absorption in the UV-VIS, the magnitude of the UV-VIS transmittance bias is equal to the UV-VIS albedo bias; since the BB transmittance bias is larger than the BB albedo bias (Fig. 8, top panel), and the NIR albedo bias contribution is proportionally smaller than the UV-VIS albedo bias contribution, the NIR contribution to the transmittance bias must exceed that of the UV-VIS.

Conclusions

We have presented an analysis of the global plane-parallel shortwave radiation bias for liquid clouds for two months, July 2003 and January 2004, using MODIS observations and a broadband radiative transfer algorithm. The biases arise from neglect of horizontal cloud optical thickness and effective radius variations at scales below ~100 km. We found that effective radius horizontal variability has a rather small effect on the albedo and transmittance bias when the optical thickness variability has already been accounted for. On the other hand, surface and atmospheric effects play a much more important role in determining the biases of full atmosphere-surface columns that contain clouds. Our estimate to of the global albedo bias (liquid cloud portion of the gridpoints only) is ~+0.03 which represents ~8% of the global liquid cloud albedo. This albedo bias translates to a global shortwave cloud radiative forcing that is stronger (i.e., more negative) by ~7-8 Wm^{-2}, assuming homogeneous conditions also for the portion of the

gridpoint not covered by liquid clouds; zonal averages of shortwave cloud radiative forcing bias can reach absolute values as high as 14 Wm^{-2} (January). These estimates can be compared with the corresponding estimates of Rossow et al. (2002) for a single day (July 15, 1986) using ISCCP cloud retrievals. Their daytime-average global value is 13 Wm^{-2}, which is larger than ours, but this is not surprising considering that it includes all cloud types and is calculated for larger areas (~300 km). Their zonal values also peak at 14 Wm^{-2}, but this value is for overcast conditions and occurs near 80° N where our July liquid cloud SWCRF bias is ~9.5 Wm^{-2}. Similarly to us, they find that the broadband atmospheric absorptance bias is roughly an order of magnitude smaller than the albedo bias. Maps of albedo bias from ISCCP can be found at http://isccp.giss.nasa.gov. While many geographical features for the low cloud category are similar to ours (Fig. 4) there are also differences that may have to do with the different reference area size, the subset of clouds considered, and the contribution of clear-sky albedo in the calculation (this is not clarified).

The substantial global magnitude of the plane-parallel bias in reflected and transmitted flux due to liquid clouds, when one considers that $SWCRF \approx -50$ Wm^{-2} globally, due to all types of clouds, stresses the importance of predicting subgrid variability in GCMs and accounting for its effects in cloud-radiation interactions. The results of this study along with those for cloud inhomogeneity derived from the same MODIS dataset (Oreopoulos and Cahalan, 2005) constitute a useful validation dataset for GCMs implementing cloud schemes with subgrid prediction capabilities at spatial resolution similar to that of MODIS Level-3. We hope to make this validation dataset more complete with ice cloud PPH bias estimates in the near future.

References

Barker, H. W., 1996: A parameterization for computing grid-averaged solar fluxes for inhomogeneous marine boundary layer clouds, part I: methodology and homogeneous biases. *J. Atmos. Sci.*, **53**, 2289-2303.

Barker H. W., and P. Räisänen, 2004: Neglect by GCMs of subgrid-scale horizontal variations in cloud-droplet effective radius: A diagnostic radiative analysis. *Q. J. R. Meteor. Soc.*, **130**, 1905-1920.

Cahalan, R. F., W. Ridgway, W. J. Wiscombe, T. L. Bell and J. B. Snider, 1994: The albedo of fractal stratocumulus clouds. *J. Atmos. Sci.*, **51,** 2434-2455.

Chou, M.-D., M. J. Suarez, C.-H. Ho. M. M.-H. Yan, and K.-T. Lee, 1998: Parameterizations for cloud overlapping and shortwave single-scattering properties for use in general circulation and cloud ensemble models. *J. Climate,* **11,** 202-214.

Derber, J. C., D. F. Parrish, and S. J. Lord, 1991: The new global operational analysis system at the National Meteorological Center. *Weath. Forec.*, **6**, 538–547.

Harshvardhan, and D. A. Randall, 1985: comments on "The parameterization of radiation for numerical weather prediction and climate models". *Mon. Wea. Rev.*, **113,** 1832-1833.

Hu, Y. X., and K. Stamnes, 1993: An accurate parameterization of the radiative properties of water clouds suitable for use in climate models. *J. Climate*, **6**, 728–742.

Khairoutdinov, M., D. A. Randall, and C. DeMott. 2005: Simulations of the Atmospheric General Circulation Using a Cloud-Resolving Model as a Superparameterization of Physical Processes. *J. Atmos. Sci.,* **62**, 2136–2154.

Kiehl, J.T. and K.E. Trenberth, 1997: Earth's annual global mean energy budget. *Bull.*

Amer. Meteor. Soc., **78**, 197–208.

King, M. D., W. P. Menzel, Y. J. Kaufman, D. Tanré, B.-C. Gao, S. Platnick, S. A. Ackerman, L. A. Remer, R. Pincus, and P. A. Hubanks, 2003: Cloud and aerosol properties, precipitable water, and profiles of temperature and water vapor from MODIS. *IEEE Trans. Geosc. Rem. Sens.*, **41**, 442-458.

Moody, E. G., M. D. King, S. Platnick, C. B. Schaaf, and F. Gao, 2005: Spatially complete global spectral surface albedos: Value-added datasets derived from Terra MODIS land products. *IEEE Trans. Geosci. Remote Sens.*, **43**, 144-158.

Oreopoulos, L., and R. Davies, 1998: Plane parallel albedo biases from satellite observations. Part I: Dependence on resolution and other factors. *J. Climate*, **11**, 919-932.

Oreopoulos, L., M.-D. Chou, M. Khairoutdinov, H. W. Barker, and R. F. Cahalan, 2004: Performance of Goddard Earth Observing System GCM Column Radiation Models under heterogeneous cloud conditions. *Atmos. Res.*, **72**, 365-382.

Oreopoulos, L., and R. F. Cahalan, 2005: Cloud inhomogeneity from MODIS. *J. Climate*, **18**, 5110–5124.

Pincus, R., S. A. McFarlane, and S. A. Klein, 1999: Albedo bias and the horizontal variability of clouds in subtropical marine boundary layers: observations from ships and satellites. *J. Geophys. Res.*, **104**, 6183-6191.

Platnick, S., M. D. King, S. A. Ackerman, W. P. Menzel, B. A. Baum, , J. C. Riédi, and R. A. Frey, 2003: The MODIS cloud products: Algorithms and examples from Terra. *IEEE Trans. Geosc. Rem. Sens.*, **41**, 459-473.

Räisänen, P., G. A. Isaac, H. W. Barker, and I. Gultepe, 2003: Solar radiative transfer for stratiform clouds with horizontal variations in liquid-water path and droplet effective

radius. *Q. J. R. Meteor. Soc.*, **129**, 2135-2149.

Räisänen, P., H. W. Barker, M. F. Khairoutdinov, J. Li, and D. A. Randall, 2004: Stochastic generation of subgrid-scale cloudy columns for large-scale models. *Quart. J. Roy. Meteor. Soc.*, **130**, 2047–2067.

Rossow, W. B., C. Delo, and B. Cairns, 2002: Implications of the observed mesoscale variations of clouds for the Earth's radiation budget. *J. Climate*, **15**, 557-585.

Stephens, G. L., 1988: Radiative transfer through arbitrarily shaped optical media. Part I: A general method of solution. *J. Atmos. Sci.*, **45**, 1818-1836.

Figure Captions

Figure 1. Top panel: Global monthly-averaged PPH albedo and B_1^R and B_2^R biases of liquid clouds from MODIS Terra and MODIS Aqua Level-3 for July 2003 and January 2004 (cloudy portion of gridpoints only). Bottom panel: Corresponding absolute values of shortwave cloud radiative forcing (SWCRF) bias B_1^{SWCRF} and B_2^{SWCRF}.

Figure 2. Broadband albedo at SZA=60° vs. r_e for clouds with visible (band 1 of our RT model) optical thickness 15 (solid line) and LWP=96 gm^{-2} (dashed line). In the latter case, cloud optical thickness varies with r_e because of changes in cloud extinction. No atmospheric effects were accounted for and the surface is black.

Figure 3. Top panel: Monthly-averaged full-column and cloud-only (vacuum) PPH albedos of liquid clouds for Northern Hemisphere land and ocean gridpoints from MODIS Terra and MODIS Aqua Level-3 for July 2003 and January 2004 (cloudy portion of gridpoints only). Bottom panel: Corresponding B_1^R biases.

Figure 4. Monthly-averaged B_1^R bias for the portion of the MODIS Terra Level-3 1°x1° gridpoints filled with liquid clouds. Atmospheric and surface effects are included. Top panel is for July 2003 and bottom panel is for January 2004.

Figure 5. Relationship between monthly-averaged χ and B_1^R from all MODIS Terra July 2003 1°x1° gridpoints with liquid clouds. Atmospheric and surface effects are included.

Figure 6. Top panel: Normalized frequency of occurrence distributions of monthly-averaged B_1^R and B_2^R biases from MODIS Terra. Bottom panel: Normalized frequency of occurrence distributions of monthly-averaged B_1^R biases from MODIS Terra and MODIS Aqua. Atmospheric and surface effects are included.

Figure 7. Top panel: Zonal variation of monthly-averaged χ for liquid clouds observed from MODIS Terra and MODIS Aqua for July 2003 and January 2004. Bottom panel: Zonal variation of absolute TOA SWCRF monthly biases B_1^{SWCRF}.

Figure 8. Top panel: Global comparisons between monthly-averaged B^R ("TOA") and B^N ("SFC") (liquid-cloud portion of gridpoints only). Bottom panel: Ratio of UV-VIS PPH biases over the total broadband biases for the cases considered in the top panel. The line indicates the fraction of solar energy in the UV-VIS region (first band of the RT algorithm). From MODIS Terra July 2003 data.

Figure 9. Top panel: Monthly-averaged atmospheric absorptance bias (B^A) versus monthly-averaged albedo bias (B^R) for Terra July 2003 and clouds in a vacuum (i.e, the atmospheric absorptance bias is equal to the cloud absorptance bias). Bottom panel: As in top panel, but with atmospheric and surface albedo effects included (i.e., the atmospheric absorptance bias corresponds to the entire atmospheric column).

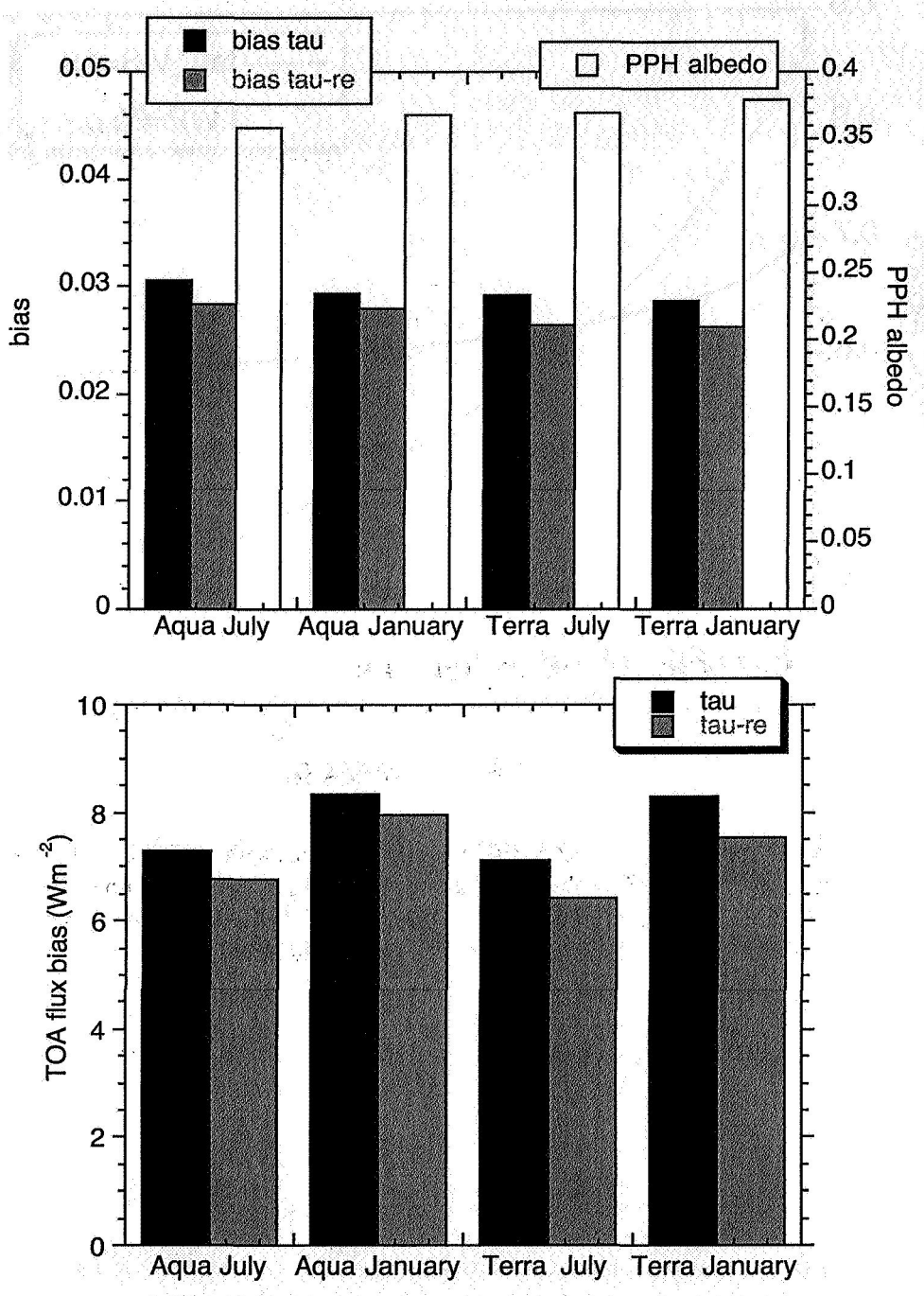

Figure 1. Top panel: Global monthly-averaged PPH albedo and B_1^R and B_2^R biases of liquid clouds from MODIS Terra and MODIS Aqua Level-3 for July 2003 and January 2004 (cloudy portion of gridpoints only). Bottom panel: Corresponding absolute values of shortwave cloud radiative forcing (SWCRF) bias B_1^{SWCRF} and B_2^{SWCRF}.

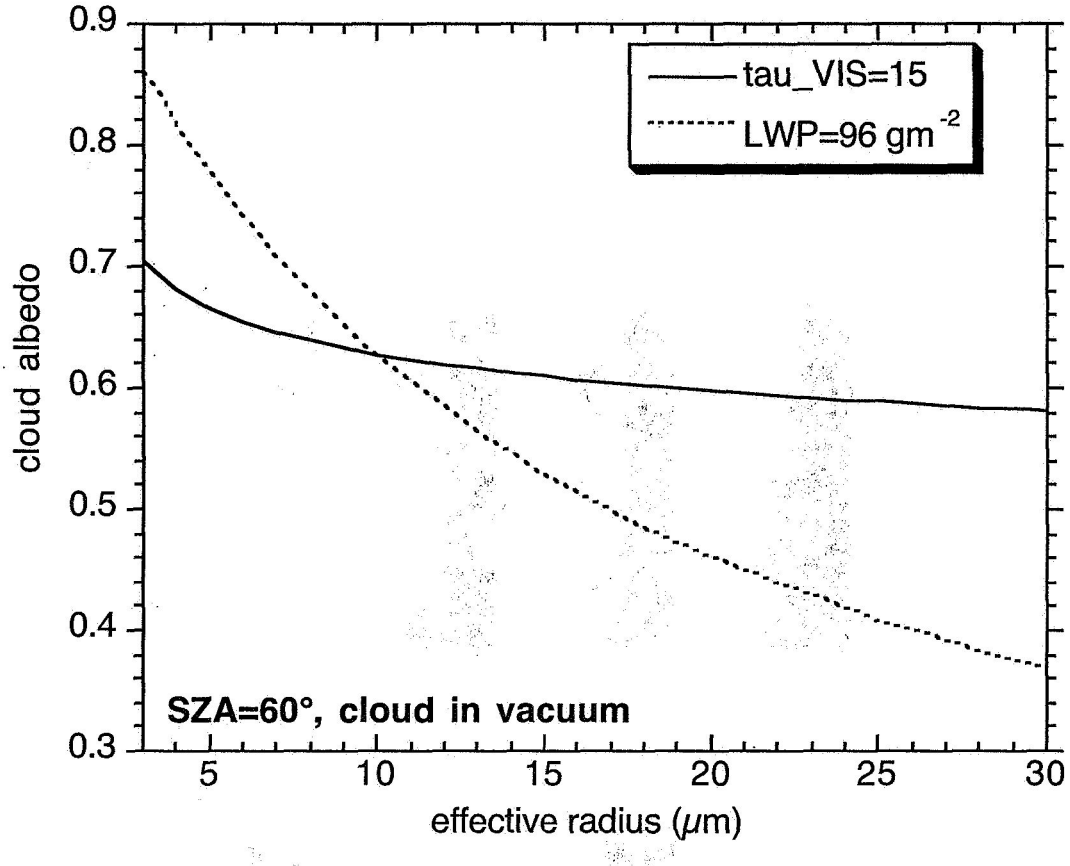

Figure 2. Broadband albedo at SZA=60° vs. r_e for clouds with visible (band 1 of our RT model) optical thickness 15 (solid line) and LWP=96 gm^{-2} (dashed line). In the latter case, cloud optical thickness varies with r_e because of changes in cloud extinction. No atmospheric effects were accounted for and the surface is black.

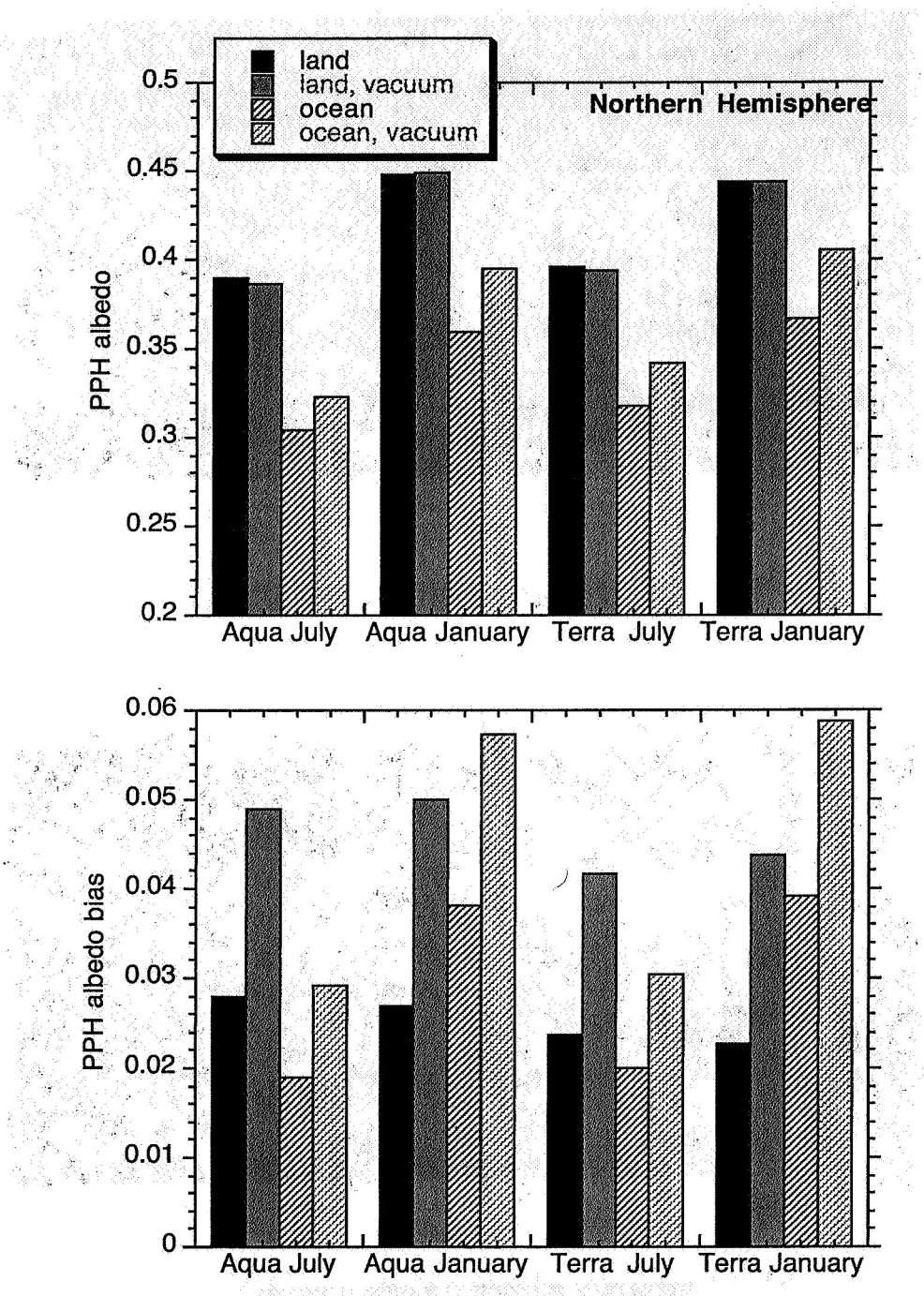

Figure 3. Top panel: Monthly-averaged full-column and cloud-only (vacuum) PPH albedos of liquid clouds for Northern Hemisphere land and ocean gridpoints from MODIS Terra and MODIS Aqua Level-3 for July 2003 and January 2004 (cloudy portion of gridpoints only). Bottom panel: Corresponding B_1^R biases.

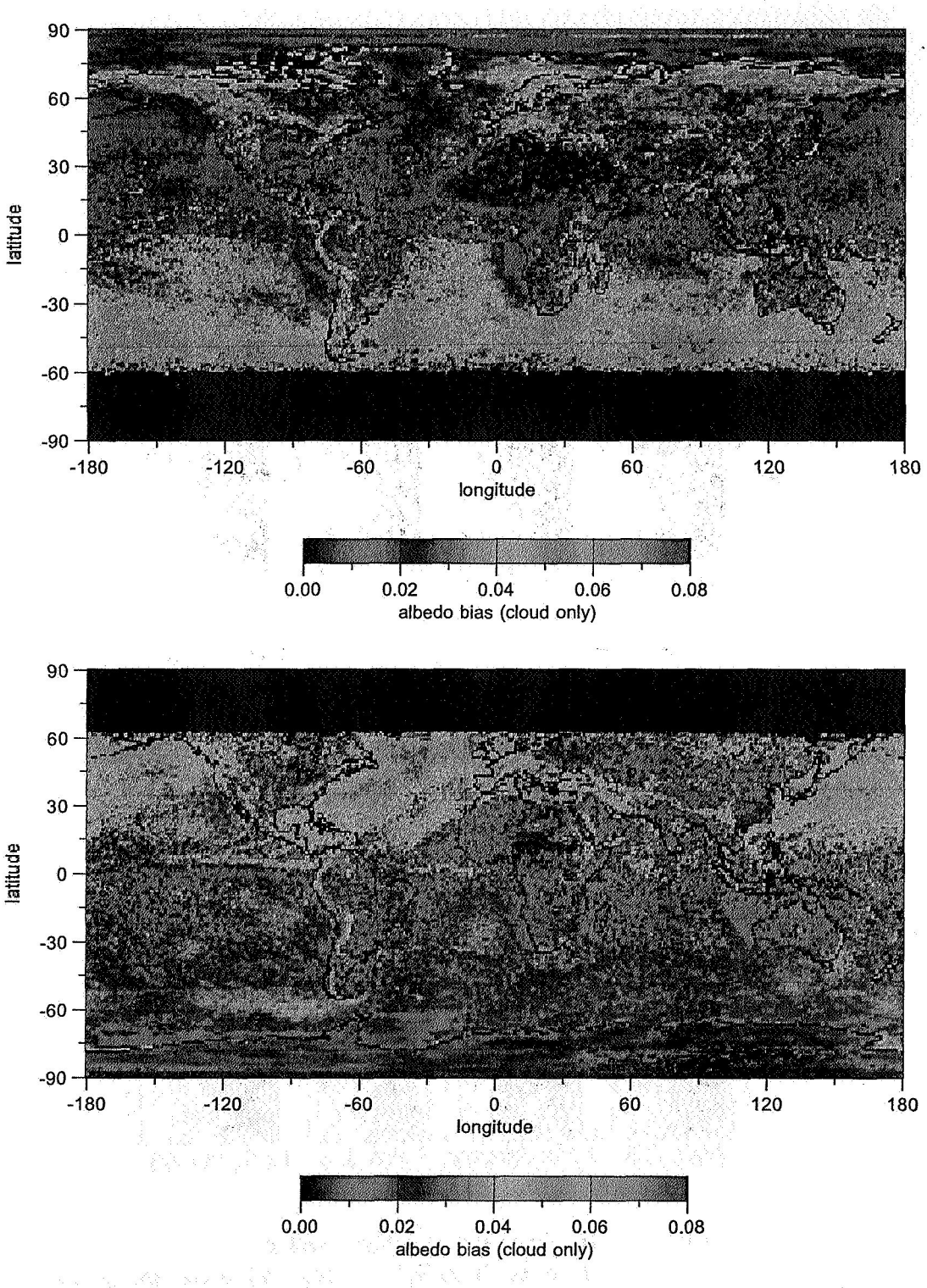

Figure 4. Monthly-averaged B_1^R bias for the portion of the MODIS Terra Level-3 1°x1° gridpoints filled with liquid clouds. Atmospheric and surface effects are included. Top panel is for July 2003 and bottom panel is for January 2004.

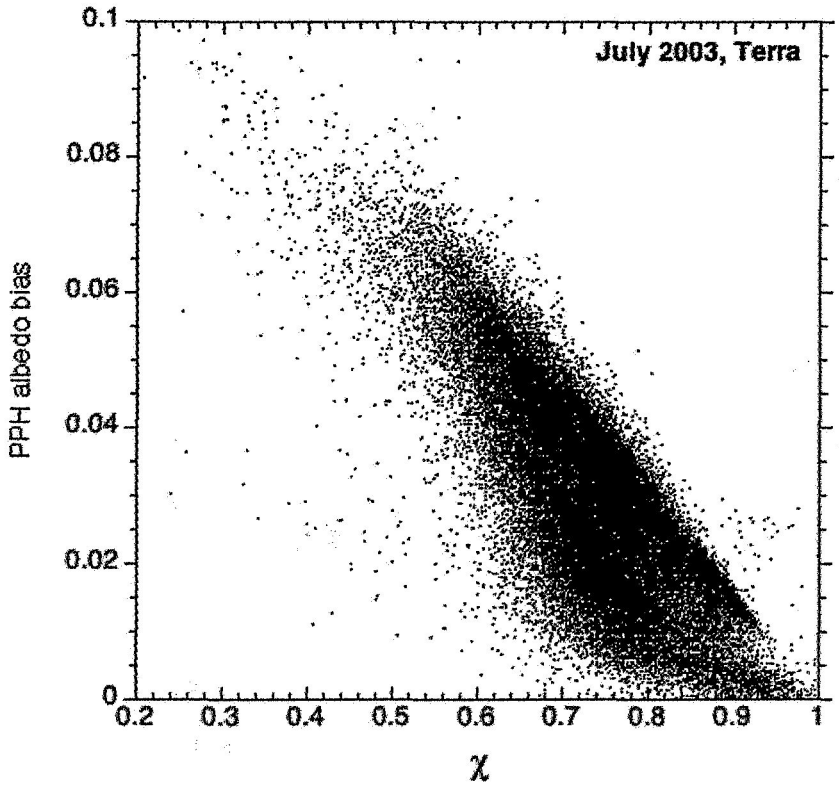

Figure 5. Relationship between monthly-averaged χ and B_1^R from all MODIS Terra July 2003 1°x1° gridpoints with liquid clouds. Atmospheric and surface effects are included.

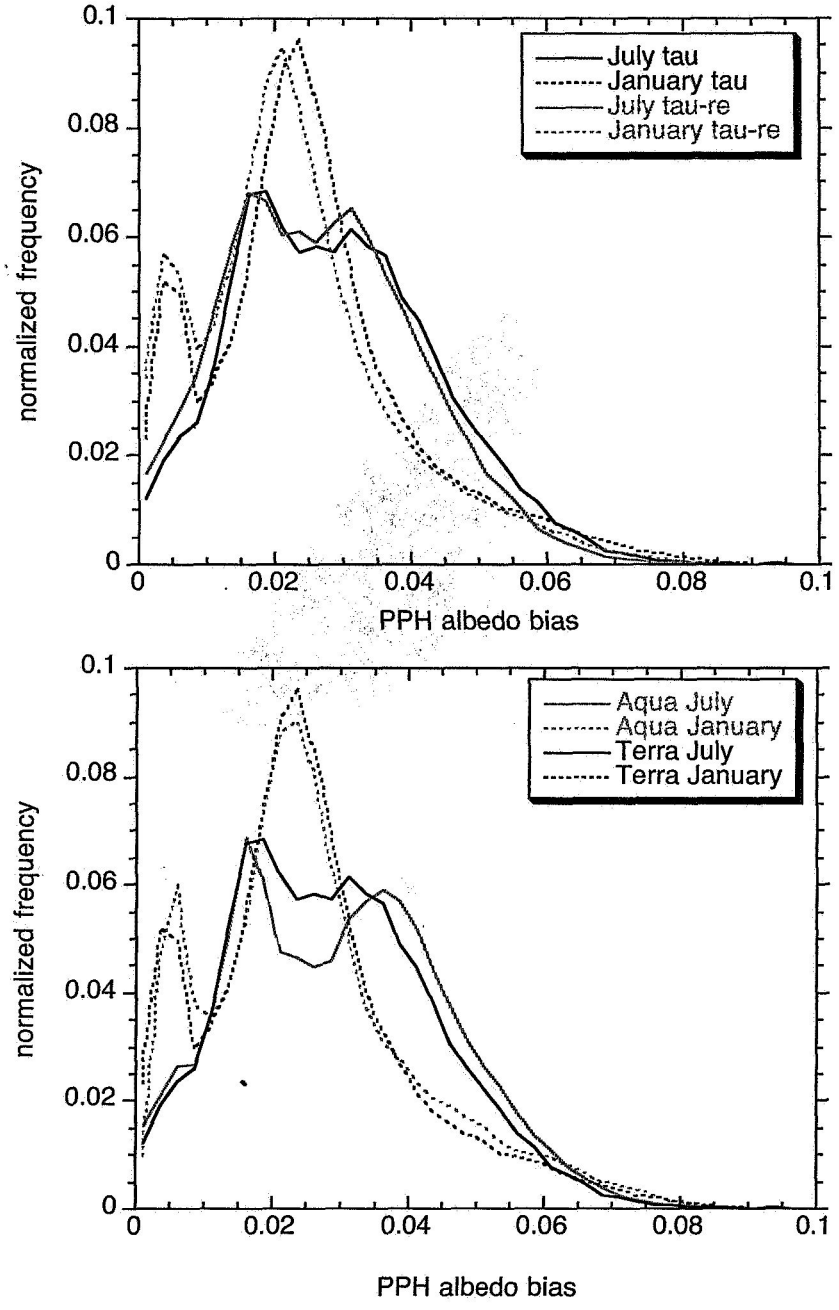

Figure 6. Top panel: Normalized frequency of occurrence distributions of monthly-averaged B_1^R and B_2^R biases from MODIS Terra. Bottom panel: Normalized frequency of occurrence distributions of monthly-averaged B_1^R biases from MODIS Terra and MODIS Aqua. Atmospheric and surface effects are included.

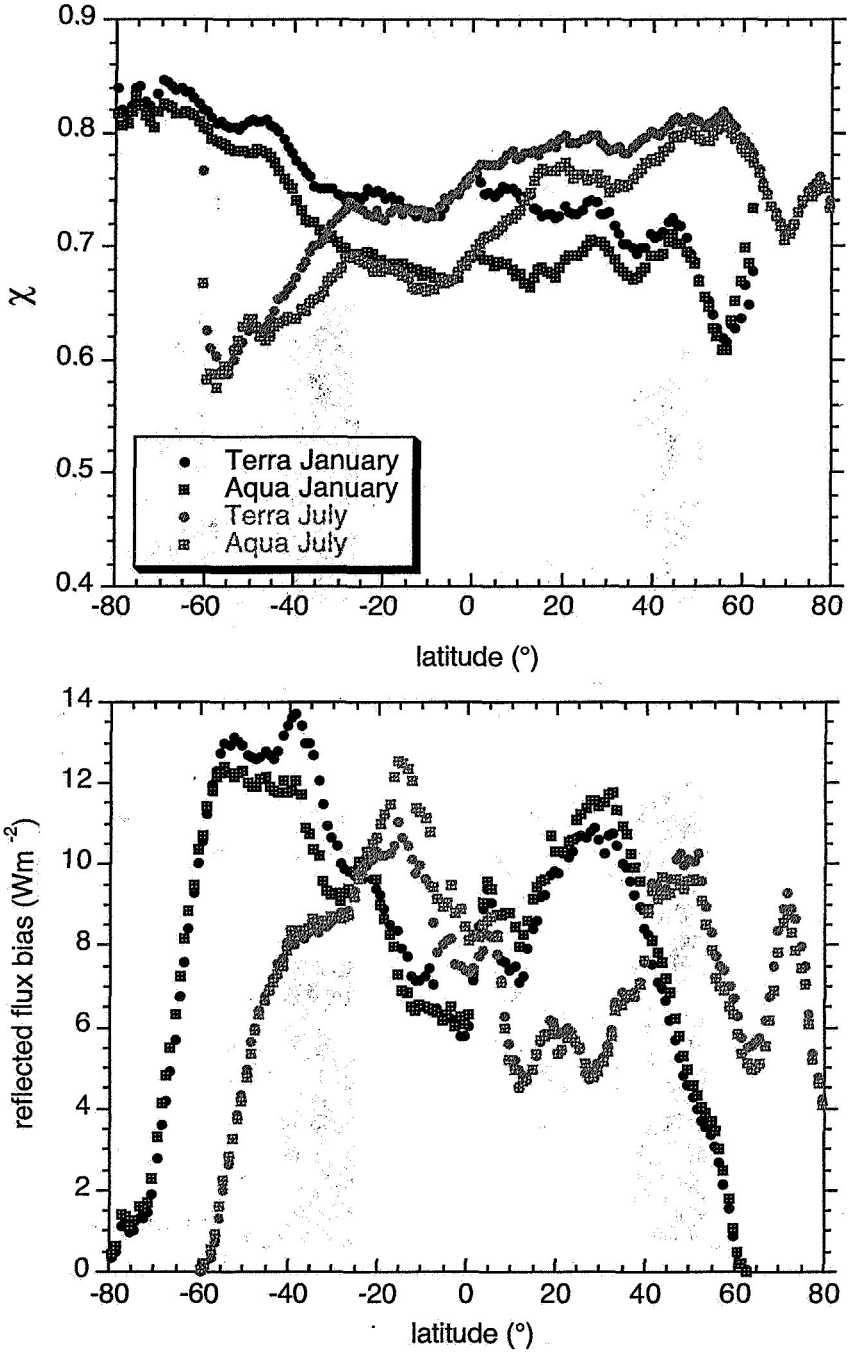

Figure 7. Top panel: Zonal variation of monthly-averaged χ for liquid clouds observed from MODIS Terra and MODIS Aqua for July 2003 and January 2004. Bottom panel: Zonal variation of absolute TOA SWCRF monthly biases B_1^{SWCRF}.

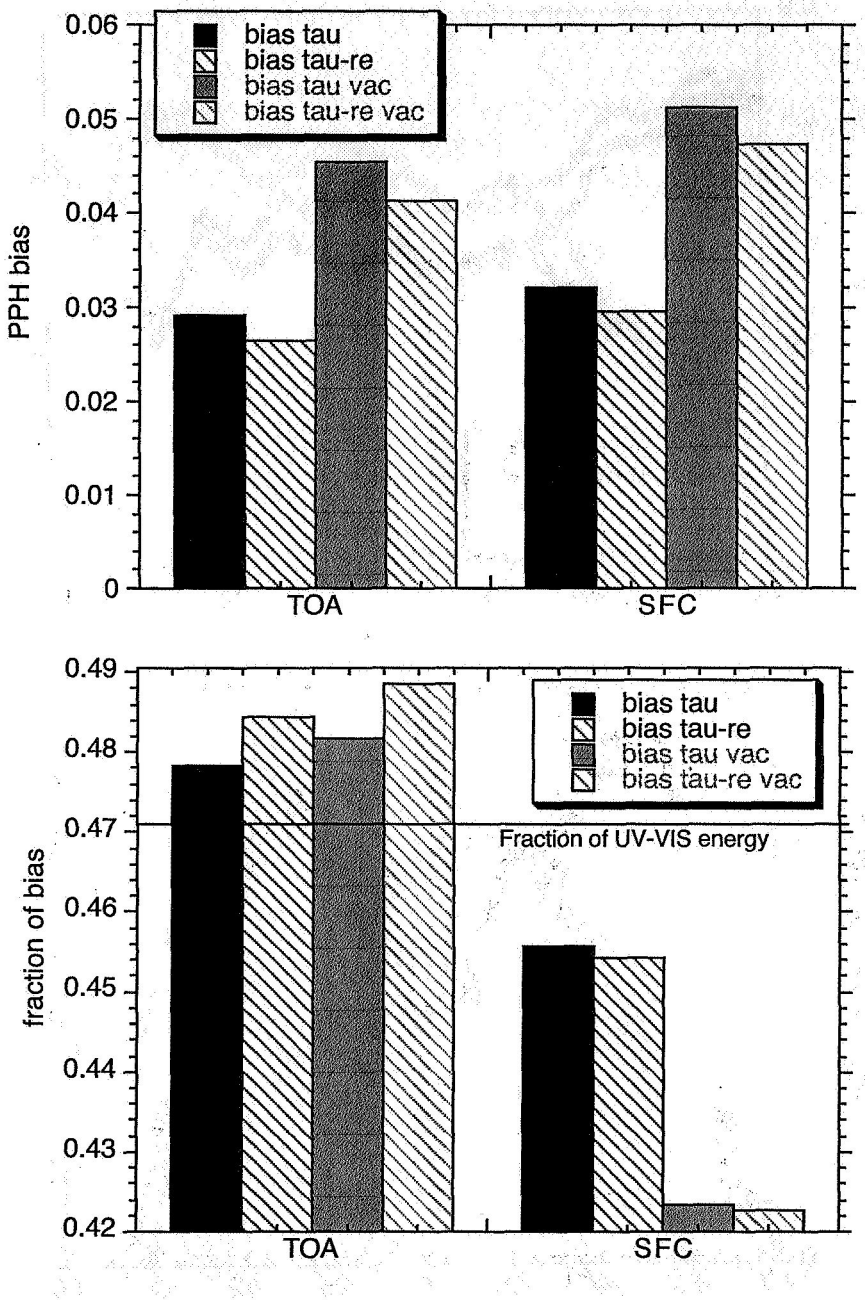

Figure 8. Top panel: Global comparisons between monthly-averaged B^R ("TOA") and B^N ("SFC") (liquid-cloud portion of gridpoints only). Bottom panel: Ratio of UV-VIS PPH biases over the total broadband biases for the cases considered in the top panel. The line indicates the fraction of solar energy in the UV-VIS region (first band of the RT algorithm). From MODIS Terra July 2003 data.

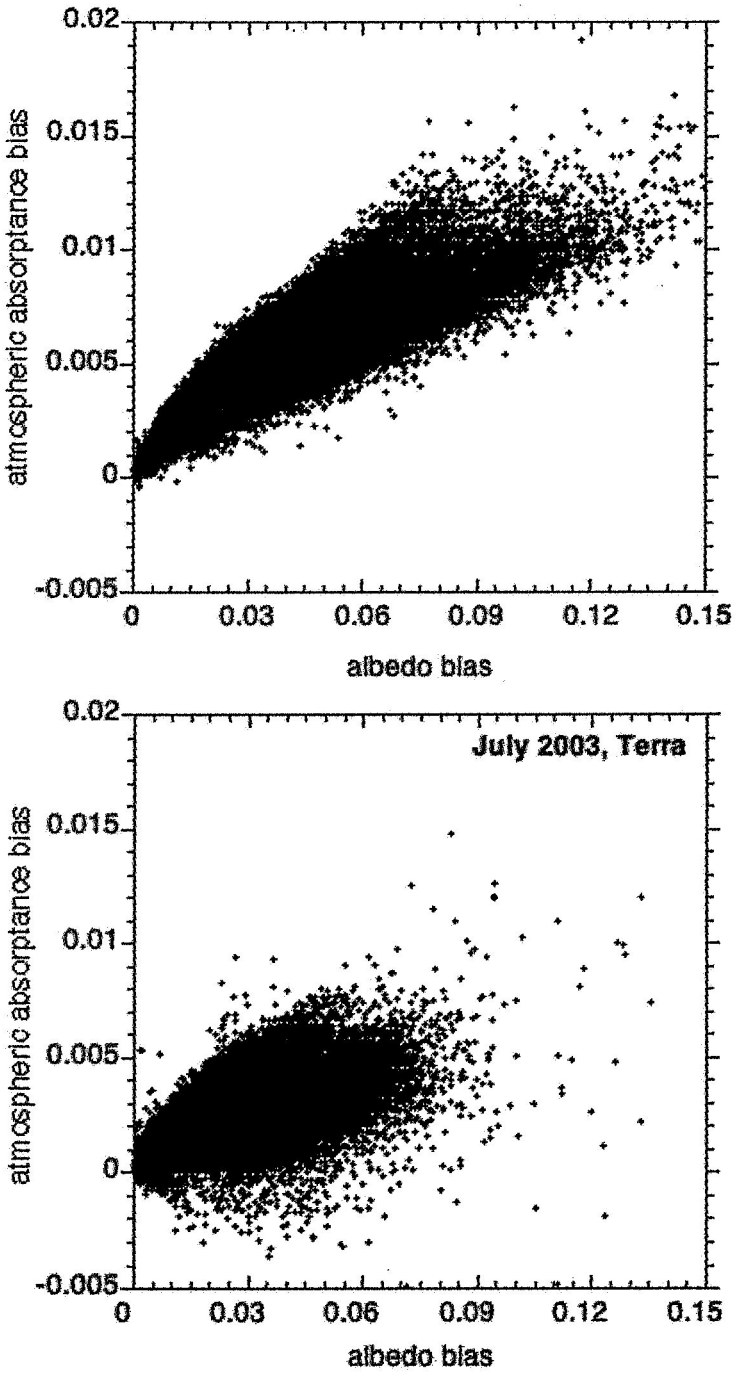

Figure 9. Top panel: Monthly-averaged atmospheric absorptance bias (B^A) versus monthly-averaged albedo bias (B^R) for Terra July 2003 and clouds in a vacuum (i.e, the atmospheric absorptance bias is equal to the cloud absorptance bias). Bottom panel: As in top panel, but with atmospheric and surface albedo effects included (i.e., the atmospheric absorptance bias corresponds to the entire atmospheric column).